AIAA JOURNAL
Vol. 43, No. 8, August 2005

Magnetoaerodynamic Actuator for Hypersonic Flow Control

J. S. Shang*
Wright State University, Dayton, Ohio 45435
and
Sergey T. Surzhikov†
Russian Academy of Sciences, 119526, Moscow, Russia

The classic pressure interaction over a sharp leading edge is a unique feature of hypersonic flow in which the boundary layer interacts strongly with the oncoming stream. The present magnetoaerodynamic actuator is based on the fact that the plasma ignited on a surface can modify the boundary-layer displacement thickness. This electromagnetic perturbation to the flowfield is further amplified by the hypersonic viscous-inviscid interaction to produce a high-surface-pressure plateau on a microsecond scale. The induced surface pressure is an effective hypersonic flow control mechanism. In essence, the minuscule magnetoaerodynamic interaction adjacent to the solid surface is introduced as an added physical mechanism for flow control. The electromagnetic force enhanced inviscid-viscous interaction generates a greater high-pressure regime over the solid surface than that of the classic hypersonic pressure interaction. This plasma actuator is demonstrated by solving the two-dimensional magnetoaerodynamic equation including the Lorentz force and Joule heating. For plasma generated by secondary electronic emission, the well-known ionization formulation for thermal excitation is inapplicable. The drift-diffusion plasma model is adopted to describe the detailed electrodynamic structure of the glow discharge. The idea of a plasma actuator has been supported by preliminary experimental data at a Mach number of five.

Nomenclature

B	=	magnetic flux density
D_a	=	ambipolar diffusion coefficient
E	=	electric field strength
j	=	electric current density
L	=	spatial scale
p	=	pressure
Q	=	heat flux
T	=	temperature
u, v	=	components of flow velocity $\boldsymbol{V}$
β	=	electron-ion recombination coefficient
λ	=	conductivity
μ	=	viscosity
μ_e	=	electron mobility
μ_+	=	ion mobility
ν_i	=	ionization frequency
ρ	=	density
σ	=	electric conductivity
φ	=	electric potential

subscripts

w	=	surface
∞	=	undisturbed stream

Introduction

RECENT research in magnetofluid dynamics has led to a better appreciation of harnessing electromagnetic-aerodynamic interaction for improving aerodynamic performance. In the past few years, innovations have been advocated for counterflow plasma injection for hypersonic flow drag reduction,[1,2] Magnetogasdynamics (MGD) flow bypass for scramjet propulsion,[3] magnetohydrodynamic mechanism for ignition and combustion stability enhancements,[4] and more recently, the use of energy deposition for flowfield control.[5] After close scrutiny, some of these ideas show potential to be revolutionary technology developments.[6–10] It is realized that the significant effect of an electromagnetic force must be built on a self-sustained and amplifiable phenomenon that is accentuated by viscous-inviscid and magnetoaerodynamic interactions. The weakly ionized hypersonic flow environment offers a realizable opportunity. For this reason, the magnetoaerodynamics interaction remains to be the most promising and vibrant technical frontier for future hypersonic flight.

In all research activities, two classic magnetofluid-dynamic similitude parameters repetitively reassert themselves as the key criteria for assessing the relative merit of technologic innovations. The magnetoaerodynamic interaction parameter $S = \sigma B^2 L/\rho u$ is the defining index for the electromagnetic force to produce a significant modification to aerodynamic behavior. For the electromagnetic force to exert a strong influence on the flowfield, the electrical conductivity of the flow medium must be sufficiently high together with a strong applied magnetic field strength. The interaction parameter has a greater value when the flight environment is in a high-altitude or low-density environment. The other similarity parameter is the magnetic Reynolds number $Re_M = \mu\sigma u L$, which establishes a measure for the ratio of the induced to total magnetic field strength. In most aerodynamic applications, this parameter has a value much less than unity.[11] In other words, in weakly ionized gases the induced magnetic field is negligible in comparison with an externally applied field.

Nearly all ground-based experimental facilities use electron collision processes for plasma generation in which the electron attains a highly excited state and the positive and negative charged ions retain the thermal condition of their ambient environment.[12] The charge number density of the nonequilibrium, weakly ionized gas is generally limited to the order of magnitude around $10^{12}/\text{cm}^3$, and the thermodynamic behavior is significantly different from the plasma generated by thermal excitation.[11,12] In computational simulation, high-temperature statistical thermodynamics with chemical kinetics developed for hypersonic flow is incapable to predict the degree of ionization for the low-temperature plasma. Therefore, an alternative approach to evaluate the degree of ionization for the low-temperature weakly ionized gas becomes necessary.

Received 21 November 2003; revision received 16 August 2004; accepted for publication 24 January 2005.

*Research Professor, Mechanical and Materials Engineering Department. Fellow AIAA.

†Professor and Head, Computational Physical-Chemical and Radiative Gasdynamics Laboratory, Institute for Problems in Mechanics. Associate Fellow AIAA.

From the most recent research result, a drift-diffusion glow discharge model has successfully simulated glow discharge phenomena even in the presence of a magnetic field.[13,14] The numerical results indicate orders-of-magnitude higher charged particle concentrations adjacent to the electrodes, thus a much greater electrical conductivity σ near the plasma sheath region. This observation is substantiated by transverse, dc discharge experiments in a Mach 5 plasma channel.[15,16] From earlier experiments, the applied magnetic field generated by a solenoid decays much faster than the inverse cubic power of distance from the magnetic pole.[6] Near the surface, a strong applied magnetic field strength can be maintained locally without an excessive power requirement. This environment of a combined high electrical conductivity and strong applied magnetic field will greatly enhance the magnetoaerodynamic interaction.

Classic hypersonic flow theory by Hayes and Probstein describes the inviscid-viscous interaction over a sharp leading edge as the pressure interaction.[17] The pressure distribution near the leading edge of a solid surface can be significantly altered by the growth rate of the displacement thickness of a boundary layer. The outward deflection of the streamlines and size of the induced high-pressure region can be manipulated to reach far downstream. The magnitude of the induced pressure is well known and can be calculated by a single interaction parameter $\bar{\chi} = M^3(C/Re_x)^{1/2}$, where $C = (\mu_w \rho_w/\mu_\infty \rho_\infty)$, and $Re_x = (\rho_\infty u_\infty x/\mu_\infty)$. The dependence on the cubic power of the freestream Mach number for the pressure interaction parameter is greatly amplified in hypersonic flows.

The ideas of using surface plasma for flow control differ significantly from most conventional plasma-based actuators including that of Leonov et al.[8] In the present approach, the viscous-inviscid interaction is a key component of the control mechanism. The surface plasma is introduced into the interacting flowfield as an electromagnetic perturbation; the ensuing viscous-inviscid interaction generates a pressure rise for the pitching moment. Therefore the electromagnetic force is only imposed as the added physical dimension for flow control to alter the boundary-layer structure. This electromagnetic perturbation is amplified by the naturally occurring aerodynamic interaction to produce a flow deflection on a fixed control surface. This effect shows itself as a pitching moment. Meanwhile, neither moving components nor parasitical appendages of the flight control system are required. A parallel experimental and computational effort is planned for this research endeavor.[15,16]

Governing Equations

For the purpose of demonstrating the hypersonic magnetoaerodynamic actuator concept, only the two-dimensional magnetoaerodynamic equations in terms of mass-averaged variables are used. Computational grid transformation is used only for the purpose of localized grid refinement at the leading edge of the plate and electrodes. The governing equations constitute the magnetoaerodynamic and electrodynamic formulations to illustrate the interrelationship and interaction between two dominant elements of the magnetoaerodynamic interaction. In classic magnetohydrodynamic numerical algorithms, a system of eight eigenvalues must be considered, which leads to a very complex formulation and computational procedure.[7] However, if one takes advantage of the low-magnetic-Reynolds-number condition to treat the Lorentz force and the Joule heating as source terms in the Navier–Stokes equations, the formulation is vastly simplified. In the present investigation, the charged particle and electrical current conservation equations are solved along with the external circuit equation to ensure a self-consistent electric field.

The weakly ionized gas is assumed to consist of three components: electrons, positive charged ions, and neutral particles. At an experimental condition of a Mach 5 plasma channel, the static temperature and pressure of the airstream is 43 K and 0.59 torr, respectively. The neutral particle number density is estimated to be $1.33 \times 10^{17}/\text{cm}^3$, and the maximum degree of ionization is of the order of magnitude of 10^{-5}. The electrical conductivity σ, measured by both Langmuir probe and microwave absorption measurement, yields a value about 0.1 Mho/m (Refs. 15 and 16). In spite of the low density level of the channel, the unit Reynolds number in the test section is 1.08×10^6 per meter to ensure that the flowfield remains in the continuum regime.

In view of the vast range of difference between the speed of light and the speed of sound, a loosely coupled and iterative scheme is adopted to solve the magnetoaerodynamic and the electrodynamic equations. The numerical result of the present effort is a steady-state asymptote after the iterative and consecutive solutions converge to a prescribed tolerance (10^{-5}).

Aerodynamic Equations

To capture strong shock waves, a flux-vector-splitting scheme is used to solve the governing equations of magnetoaerodynamics.[9] At the low magnetic Reynolds condition, the magnetoaerodynamic equations are essentially the Navier–Stokes equations with the Lorentz force and Joule heating appearing as source terms in the momentum and energy equation respectively. Therefore, the solving schemes developed in computational fluid dynamics are equally effective for these governing equations.

Continuity and conservation of momentum for the low-magnetic-Reynolds-number magnetoaerodynamic equations in a Cartesian coordinate system are given as follows:

$$\frac{\partial \boldsymbol{f}}{\partial t} + \frac{\partial \boldsymbol{E}}{\partial x} + \frac{\partial \boldsymbol{F}}{\partial y} = \frac{\partial \boldsymbol{E}_v}{\partial x} + \frac{\partial \boldsymbol{F}_v}{\partial y} + \boldsymbol{\Phi}$$

$$\boldsymbol{f} = \begin{bmatrix} \rho \\ \rho u \\ \rho v \end{bmatrix}, \qquad \boldsymbol{E} = \begin{bmatrix} \rho u \\ \rho uu + p \\ \rho uv \end{bmatrix}, \qquad \boldsymbol{F} = \begin{bmatrix} \rho v \\ \rho vu \\ \rho vv + p \end{bmatrix}$$

$$\boldsymbol{F}_v = \frac{1}{Re}\begin{bmatrix} 0 \\ \tau_{xx} \\ \tau_{xy} \end{bmatrix}, \qquad \boldsymbol{E}_v = \frac{1}{Re}\begin{bmatrix} 0 \\ \tau_{xy} \\ \tau_{yy} \end{bmatrix}, \qquad \boldsymbol{\Phi} = \begin{bmatrix} 0 \\ F_{M,x} \\ F_{M,y} \end{bmatrix}$$

$$\tau_{xx} = \mu\left[2\frac{\partial u}{\partial x} - \frac{2}{3}\left(\frac{\partial u}{\partial x} + \frac{\partial v}{\partial y}\right)\right], \qquad \tau_{xy} = \mu\left(\frac{\partial u}{\partial y} + \frac{\partial v}{\partial x}\right)$$

$$\tau_{yy} = \mu\left[2\frac{\partial v}{\partial y} - \frac{2}{3}\left(\frac{\partial u}{\partial x} + \frac{\partial v}{\partial y}\right)\right] \tag{1}$$

where $F_{M,x}$ and $F_{M,y}$ are the components of the Lorentz force. In the present approach, the temperature is chosen as the dependent variable for the energy conservation law, and this equation is cast in the nonconservative form as

$$\rho c_p \frac{\partial T}{\partial t} + \rho c_p u \frac{\partial T}{\partial x} + \rho c_p v \frac{\partial T}{\partial y} = \frac{1}{RePr}\frac{\partial}{\partial x}\left(\lambda \frac{\partial T}{\partial x}\right)$$

$$+ \frac{1}{RePr}\frac{\partial}{\partial y}\left(\lambda \frac{\partial T}{\partial y}\right) + Q_J \frac{L}{\rho_\infty u_\infty c_{p\infty} T_\infty} + Q_p + Q_\mu \tag{2}$$

where $Pr = (\mu_\infty c_{p\infty}/\lambda_\infty)$ is the Prandtl number. Functions Q_i on the right-hand side of Eq. (2) contains source terms describing the heat transfer in the control volume; Q_J is the heat release caused by Joule heating, Q_p is the heat release caused by compressibility of the gas, and Q_μ is the heat release due to viscous dissipation.

The last two terms can be presented in the following form:

$$Q_p = u\frac{\partial p}{\partial x} + v\frac{\partial p}{\partial y} \tag{3}$$

$$Q_\mu = \mu\left\{2\left[\left(\frac{\partial u}{\partial x}\right)^2 + \left(\frac{\partial v}{\partial y}\right)^2\right] + \left[\frac{\partial u}{\partial y} + \frac{\partial v}{\partial x}\right]^2 - \frac{2}{3}\left(\frac{\partial u}{\partial x} + \frac{\partial v}{\partial y}\right)\right\} \tag{4}$$

The term Q_J in the present analysis includes the Joule heating $Q_J = \eta(\boldsymbol{j} \cdot \boldsymbol{E})$, where $\boldsymbol{j}$ and $\boldsymbol{E}$ denote vectors of electric current density and electrical field intensity. In this expression η is the part of the Joule dissipation that converts the electromagnetic energy into

thermal energy. Another part of the electromagnetic energy is spent on excitation of the vibrational molecular states. It is known from the laser physics[12] that the value of η for molecular nitrogen has the range of $0.15 < \eta < 0.75$ (Ref. 13).

Electrodynamics Equations

As has been mentioned already, the electrodynamic equations are based on the global quasi-neutral drift-diffusion theory for the glow discharge plasma in a gas flow.[12] This model has been successfully demonstrated to model the glow discharge over a wide range of flow regimes.[18,19]

It is well known[20] that all parameters of the model must be modified in the presence of a magnetic field. Nevertheless it can be shown that for the present simulation conditions with an externally applied magnetic field up to 0.2 T one can neglect the magnetic field in calculating the ambipolar coefficient in the shock layer. Some decrease of electronic mobility and ionization frequency in a quasi-neutral plasma leads to a change in the voltage drop of the discharge between the electrodes and induced magnetic forces.

For the present purpose, the governing equations consist of the species concentration equation for the charged particles and continuity equation for the current density, from which one can calculate self-consistent electric field intensity. The basic formulation is presented in the following:

$$\frac{\partial \boldsymbol{f}_M}{\partial t} + \frac{\partial \boldsymbol{E}_M}{\partial x} + \frac{\partial \boldsymbol{G}_M}{\partial y} = \frac{\partial \boldsymbol{E}_{D,M}}{\partial x} + \frac{\partial \boldsymbol{G}_{D,M}}{\partial y} + \boldsymbol{Q}_M \tag{5}$$

where

$$\boldsymbol{f}_M = \begin{bmatrix} n \\ \varphi \end{bmatrix}, \qquad \boldsymbol{E}_M = \begin{bmatrix} nu \\ 0 \end{bmatrix}, \qquad \boldsymbol{G}_M = \begin{bmatrix} nv \\ 0 \end{bmatrix}$$

$$\boldsymbol{E}_{D,M} = \begin{bmatrix} D_a \dfrac{\partial n}{\partial x} \\ n\mu_e \dfrac{\partial \varphi}{\partial x} \end{bmatrix}, \qquad \boldsymbol{F}_{D,M} = \begin{bmatrix} D_a \dfrac{\partial n}{\partial y} \\ n\mu_e \dfrac{\partial \varphi}{\partial y} \end{bmatrix}$$

$$\boldsymbol{Q}_M = \begin{bmatrix} n\nu_i - \beta n^2 \\ -D_a \dfrac{\partial n}{\partial x} - D_a \dfrac{\partial n}{\partial y} \end{bmatrix}$$

$$\boldsymbol{E} = -\operatorname{grad} \varphi$$

The Lorentz force $\boldsymbol{F}_M$ is calculated as

$$\boldsymbol{F}_M = [\boldsymbol{j} \times \boldsymbol{B}] = \begin{bmatrix} \boldsymbol{e}_x & \boldsymbol{e}_y & \boldsymbol{e}_z \\ j_x & j_y & j_z \\ 0 & 0 & B \end{bmatrix} = \boldsymbol{e}_x(j_y B) - \boldsymbol{e}_y(j_x B) \tag{6}$$

Dimensions of all pertaining variables used in this computation are the following: the current density is $j \sim en\mu_e E$, A/cm^3 where $[\mu_e] = \text{cm}^2/\text{s} \cdot \text{V}$, $[E] = \text{V/cm}$. The Joule heating is $Q_J \sim \eta en\mu_e E^2$, W/cm^3. The magnetic force is designated as $f_M \sim 10^5 \chi en\mu_e EB$, g/cm $\cdot$ s^2, and the magnetic field strength is given in teslas.

Initial Values and Boundary Conditions

The initial values and boundary conditions for the system of equations are straightforward. Figure 1 depicts the investigated configuration with the embedded electrodes parallel to the leading edge. For aerodynamic variables, the no-slip condition for the velocity components, the vanishing pressure gradient condition, as well as the prescribed surface temperature or the adiabatic condition are imposed on the solid surface. For the electromagnetic variables, the tangential components of the electric intensity and the normal component of the magnetic field are allowed to continuously pass through the media interface. The normal component of the electric field intensity and tangential components of the magnetic field

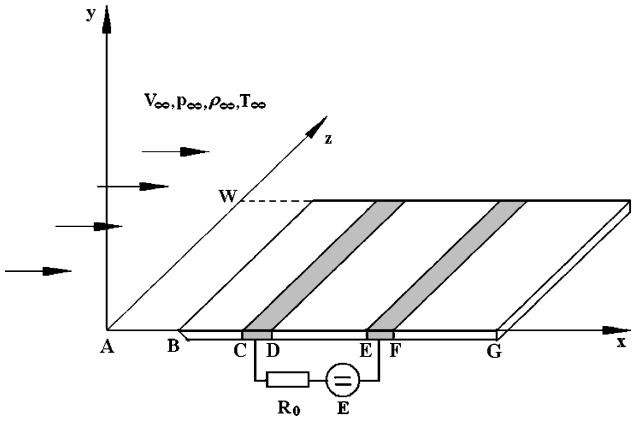

Fig. 1 Schematic of electromagnetic-fluid-dynamic actuator.

must be balanced by the surface charge density and surface current respectively at the interface.[7]

In the present analysis, with an ambient pressure over 1 torr, the Debye length is less then 10^{-4} m except at the sharp corners of the electrodes. This means that the quasi-neutral model can still be applied. The specific boundary conditions on the computational domain are prescribed as follows.

At $x = 0$:

$$u = u_\infty, \quad v = 0, \quad T = T_\infty, \quad \rho = \rho_\infty, \quad n = n_\infty, \quad \frac{\partial \varphi}{\partial x} = 0 \tag{7}$$

At $x = x_G$:

$$\frac{\partial u}{\partial x} = \frac{\partial v}{\partial x} = \frac{\partial T}{\partial x} = \frac{\partial n}{\partial x} = \frac{\partial \rho}{\partial x} = \frac{\partial \varphi}{\partial x} = 0 \tag{8}$$

At $y = 0$:

$$u = v = 0, \qquad \frac{\partial p}{\partial y} = 0 \tag{9}$$

For $x_C \le x \le x_D$ (cathode):

$$T = T_w, \qquad \frac{\partial n}{\partial y} = 0, \qquad \varphi = 0$$

For $x_E \le x \le x_F$ (anode):

$$T = T_w, \qquad \frac{\partial n}{\partial y} = 0, \qquad \varphi = V_A$$

For $x_B \le x < x_C$, $x_D < x < x_E$, $x_F < x \le x_G$ (dielectric surface):

$$n = 10^{-5} n_0, \qquad \frac{\partial T}{\partial y} = \frac{\partial \varphi}{\partial y} = 0$$

where n_0 is the typical concentration of charged particles in the positive column ($n_0 \approx 10^{10}$ cm^{-3}) and V_A is the anode potential relative to the cathode which is grounded.

The electric field intensity is obtained from the external electric circuit equation, $IR_0 + V_A = \text{emf} = E$, from which an anode voltage drop V_A can be determined. Here R_0 is the ballast resistance, and I is the total current in the circuit, which in its turn can be calculated as follows;

$$I = \int_{x \in [x_C, x_D]} j \, \mathrm{d}x = \int_{x \in [x_E, x_F]} j \, \mathrm{d}x \tag{10}$$

For the present investigation, a small electromagnetic perturbation is introduced into the Navier–Stokes solution as the initial values for the magnetoaerodynamic interaction.

Constitutive Relationships

The constitutive relationships for the magnetoaerodynamic equations in centimeter-gram-second (CGS) units are the viscosity coefficient μ and molecular thermal conductivity λ (Refs. 11, 13, and 18):

$$\mu = 2.6710^{-5}\sqrt{M_A T}\,\frac{1}{\tilde{\sigma}^2\Omega^{(2,2)*}}, \qquad \tilde{\sigma} = 3.68\text{Å}$$

$$\Omega^{(2,2)*} = 1.157(T^*)^{-0.1472}, \qquad T^* = \frac{T}{(\varepsilon/k)}, \qquad \left(\frac{\varepsilon}{k}\right) = 71.4$$

$$\lambda = 8.334\times 10^{-4}\sqrt{\frac{T}{M_A}}\,\frac{0.115 + 0.354(c_p/R_0)M_A}{\sigma^2\Omega^{(2,2)*}} \tag{11}$$

where c_p is the specific heat at constant pressure, $M_A = 29$ g/mole, and $R_0 = 8.314\times 10^7$ erg/(mole K) is the universal gas constant.

The constitutive relationships of the electrodynamic equations are for the species concentration equation, which require the Townsend and recombination coefficients α and β. The approximations for the transport properties of electrons and ions are also given:

$$v_i = (\alpha/p^*)p^*E\mu_e(p^*), \qquad (\alpha/p^*) = A\exp -[B/(E/p^*)]$$

$$p^* = p(293/T) \tag{12}$$

$$D_e = \mu_e(p^*)T_e, \qquad D_+ = \mu_+(p^*)T_+$$

$$\mu_e(p^*) = 4.2\times 10^5(1/p^*), \qquad \mu_+(p^*) = 1450(1/p^*) \tag{13}$$

where

$$\beta = 8\times 10^{-6}\,\text{cm}^3/\text{s}, \qquad T_e = 11{,}610\ \text{K}$$

$$A = 15\,(\text{cm}\cdot\text{torr})^{-1}, \qquad B = 365\ \text{V}/(\text{cm}\cdot\text{torr})$$

and $N = 0.954\times 10^{19}(p/T)$ is the concentration of the neutral particles. The use of empirical coefficients describing the physical-chemical kinetics in a glow discharge allows realistic initial conditions for a computing simulation.[12] An effective coefficient of recombination β can be used because air is an electronegative gas.[12,14]

Numerical Procedure

The present numerical procedure has the following two peculiar properties: first, the energy conservation equation is cast in nonconservative form, and second, at each time step two subiterations must be performed. In the first step, the momentum and continuity equations are integrated by an explicit method. The system of magnetoaerodynamic equations is solved by the van Leer second-order splitting method.[21] The second step is the integration of the energy conservation equation and continuity of charged particles in an electric field by an implicit method. Calculations were performed on a clustered grid.[18,19]

For the nonconservative energy equation and the electromagnetic equations, the five-point scheme was used:

$$A_{i,j}T^{n+1}_{i-1,j} + B_{i,j}T^{n+1}_{i+1,j} + A^*_{i,j}T^{n+1}_{i,j-1} + B^*_{i,j}T^{n+1}_{i,j+1} - C_{i,j}T^{n+1}_{i,j} + F_{i,j} = 0 \tag{14}$$

where

$$A_{i,j} = \left[a^+_L(\rho c_p)_{i-1,j}\big/ p_i\right], \qquad B_{i,j} = -\left[a^-_R(\rho c_p)_{i+1,j}\big/ p_i\right]$$

$$A^*_{i,j} = \left[b^+_L(\rho c_p)_{i,j-1}\big/ q_j\right], \qquad B^*_{i,j} = -\left[b^-_R(\rho c_p)_{i,j+1}\big/ q_j\right]$$

$$C_{i,j} = A_{i,j} + B_{i,j} + A^*_{i,j} + B^*_{i,j} + (\rho c_p)_{i,j}(1/\tau)$$

$$a^\pm_R = \tfrac{1}{2}\left(v_{i+\frac{1}{2},j} \pm \left|v_{i+\frac{1}{2},j}\right|\right), \qquad a^\pm_L = \tfrac{1}{2}\left(v_{i-\frac{1}{2},j} \pm \left|v_{i-\frac{1}{2},j}\right|\right)$$

$$b^\pm_R = \tfrac{1}{2}\left(u_{i,j+\frac{1}{2}} \pm \left|u_{i,j+\frac{1}{2}}\right|\right), \qquad b^\pm_L = \tfrac{1}{2}\left(u_{i,j-\frac{1}{2}} \pm \left|u_{i,j-\frac{1}{2}}\right|\right)$$

Numerical Accuracy Assessment

To demonstrate for the first time a unique flow control concept by using electromagnetic force, a side-by-side computational and experimental effort becomes essential. In particular, the present investigation is a path-finding effort that ventures into a technical area involving significant uncertainty. For this reason, all simulations were performed on two simple flat-plate models with an identical configuration but slightly different physical dimensions.[15,16] The first model has a dimension of 75×56 mm with the electrode dimensions of 51×6.4 mm. The cathode is placed at a distance of 22 mm from the sharp leading edge of the plate, and the anode is located at a distance 51 mm downstream. The second model has an even smaller physical dimension of 38×67 mm with electrode dimensions of 32×6.4 mm and three surface pressure ports of 2 mm in diameter. The cathode is placed a short distance of 22.3 mm downstream of the sharp leading edge, and the separation distance between the electrodes is 30.5 mm. The surface-pressure orifices are also located on the model centerline at distances of 34.9, 47.6, and 60.3 mm from the leading ledge. The static pressure is individually measured by three MKS Baratron 722A transducers and has been calibrated to yield an accuracy of 0.5% over the range from 0.001 to 2.0 torr (Refs. 15 and 16). For the present effort, the measured surface-pressure data are adopted as a part of validating basis.

All numerical simulations were conducted in the identical flow condition of a Mach 5 plasma channel.[16] This blowdown channel produces a freejet of a Mach number of 5.15 expanding from the stagnation pressure of 49.3 kPa and stagnation temperature of 294 K, respectively. Although the test section has a relatively small inviscid core of $120\times 100\times 50$ mm (x, y, z), the flowfield is uniform and free from a significant streamwise gradient. The unperturbed jet stream is characterized by a static pressure of 78.4 Pa (0.59 torr), a temperature of 43 K, and a velocity of 675.5 m/s. Under these flow conditions, the Reynolds number per meter is 1.615×10^5. The surface plasma is generated by a Universal Voltronics dc power supply that can deliver a current 800 mA up to 10 kV.

The behavior of the strong inviscid-viscous interaction near a sharp leading-edge wedge at the zero incident angle is clearly demonstrated by the schlieren picture in Fig. 2. This image is recorded at the freestream Mach number of 5.15, and the Reynolds number based on the length of the plate model is 1.2×10^5. Thus the boundary layer over the flat upper surface of the model is expected to be laminar. The growth of the displacement thickness of the boundary layer clearly deflects the stream outward and induces a pressure over the upper flat surface. This classic hypersonic inviscid-viscous interaction indeed generates an oblique shock over the flat-plate surface of the model. At the trailing edge of the model, the pressure interaction parameter χ with the Chapman–Rubeson constant C of unity is 0.41. In this photograph, the boundary layers leave the model surface and continue as a free shear downstream.

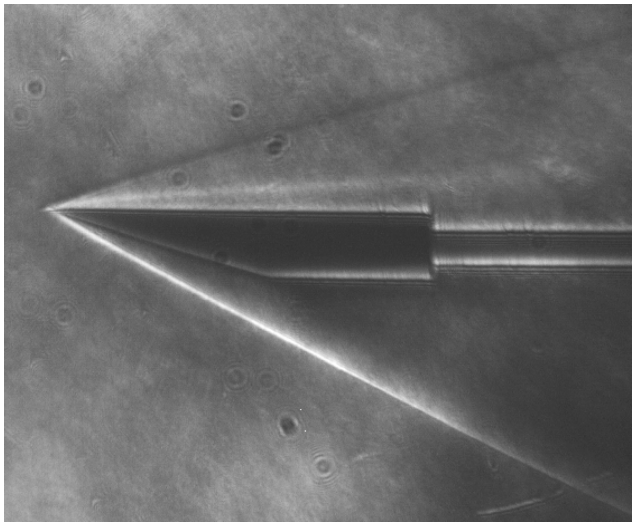

Fig. 2 Shock and shear layer structure of a wedge at $M = 5.15$.

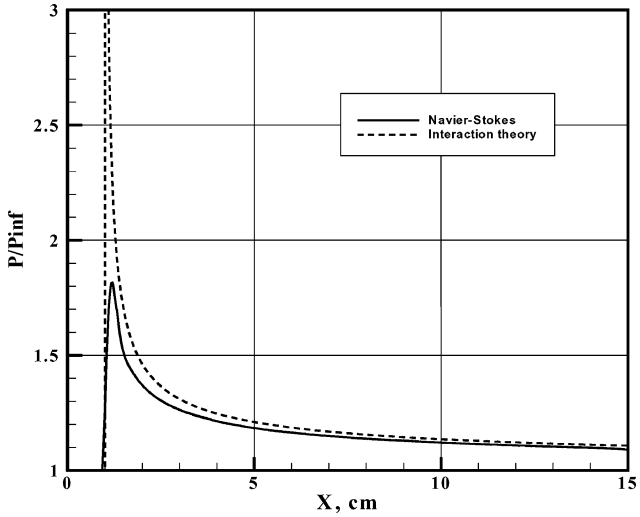

Fig. 3 Comparison with classic pressure interaction theory.

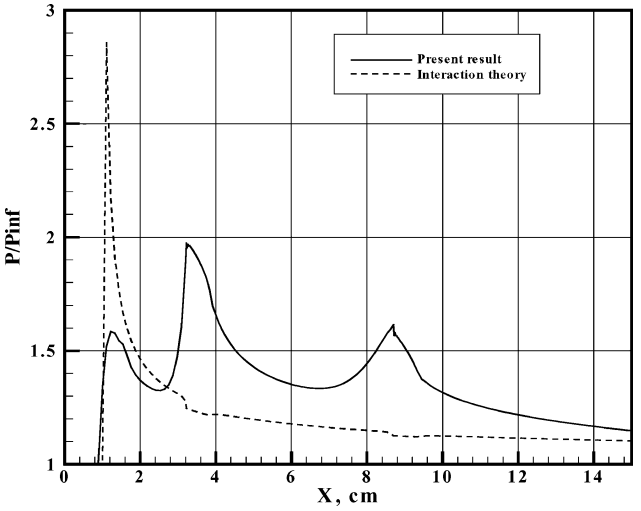

Fig. 4 Comparison of glow discharge induced pressure interaction with interaction theory.

In Fig. 3, the surface-pressure distributions over the upper flat surface of the first model were presented and compared with the classic pressure interaction theory.[17] A series of grid refinements for the viscous-inviscid interaction were performed. The grid density varies from (201×51) to (700×100). It was found that the numerical results were essentially grid independent for a mesh system of 35,000 points with a clustering in the high gradient domains. Thus, all numerical results were generated on a (500×70) grid system with high grid density at the leading edges of the plate and electrodes. For the flow condition described before, the calculated plate surface pressure at the leading edge approaches twice the value of the freestream. The pressure decays asymptotically toward its freestream value far downstream. In spite of the pressure interaction, the displacement thickness of the boundary layer still grows proportional to the square root of the distance from the leading edge. The present numerical result substantiates this observation, agreeing perfectly with the weak pressure interaction data.[17]

Glow Discharge Interaction

The present investigation demonstrates that the aerodynamic-electromagnetic interaction can be developed into a magnetoaerodynamic actuator for flow control. This notion is based on the fact that an electromagnetic perturbation can easily modify the growth rate of the displacement thickness in two respects: changing the kinematics of the field structure and initiating a heat exchange in the glow discharge region. When electrodes for plasma generation are embedded in the model surface, the electrode and Joule heating is substantial. In turn, the plasma heating will affect the thermal and velocity profile of the boundary layer. The change induced by the electromagnetic field can be significant even with a limited amount of energy input. The ensuing inviscid-viscous interaction will greatly amplify the electromagnetic perturbation in a hypersonic stream.

In earlier research efforts of glow discharges, the separation distance between the electrodes and the segmented electrodes have shown significant effect in modifying the magneto-fluid-dynamic interaction.[15,16] In Fig. 4, the surface-pressure distribution generated by a dc discharge is depicted for the large model (model 1) without an applied magnetic field. This glow discharge simulation duplicates the experimental environment in the MHD channel. The electrodes are assumed to operate at a surface temperature of 600 K. The glow discharge is maintained at an applied electrical field of 1.2 kV over an electrical resistance of 12 kΩ. The controlled electrical current transmitted between the electrodes is 50 mA. At this minuscule power input, the flow control effectiveness that is quantified by the integrated aerodynamic force over the plate surface is nearly double to that without the plasma actuator.

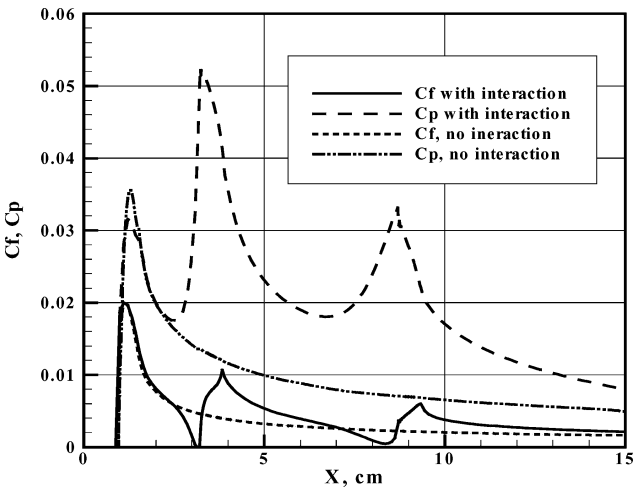

Fig. 5 Aerodynamic forces produced by direct current discharge (DCD) induced pressure interaction.

In Fig. 5, the resultant aerodynamic forces measured by the pressure and skin friction coefficients are presented. The steep adverse pressure gradients upstream of the electrodes almost produce flow separations locally as predicted by the two-dimensional simulation. In this computation, only the glow discharge is ignited. Because the external magnetic field is absent, the Lorentz force is negligible. The measured surface pressure is higher than the well-known classic pressure interaction that consists of only an expanding flowfield from the leading edge. The modified boundary-layer structure by the surface plasma induces a rather complex compression and expansion region between the electrodes, and the surface shear stress must adjust accordingly. In short, the perturbation by electromagnetic forces is significant and can be easily elevated by either increasing the glow discharge power input or implementing a series of electrodes.[18,19] In the experimental effort, by doubling the discharge electric current to 100 mA, a significant increase in induced pressure was noticed.[16]

In supersonic and hypersonic flows, the pressure contour is an excellent description of shock-wave structure. The shock structure at the leading edge and its modifications by the discharging electrodes is detectable in Fig. 6. Instead of expanding continuously from the leading edge toward the downstream of the plate, secondary compression waves coalesce at the leading edges of the cathode and anode and are partitioned by an expansion region between the electrodes. This observation is substantiated by the surface-pressure distribution over the entire plate shown in Fig. 4. The increased

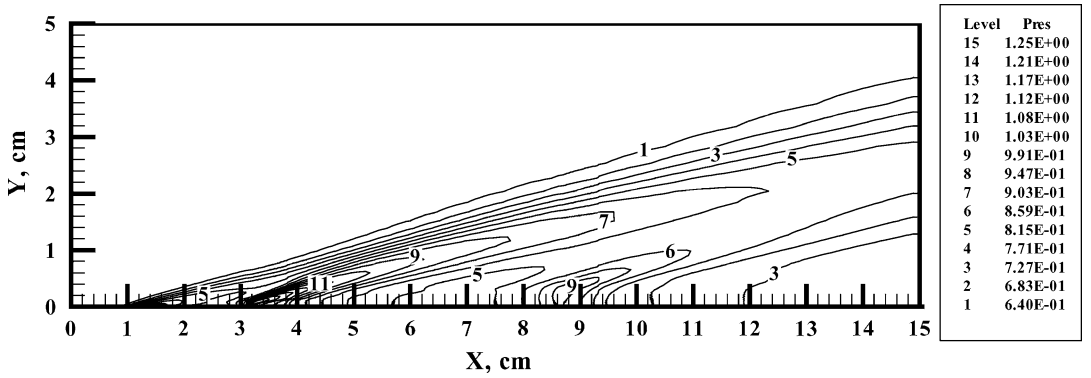

Fig. 6 Shock-wave structure over glow discharge plate, p in torr.

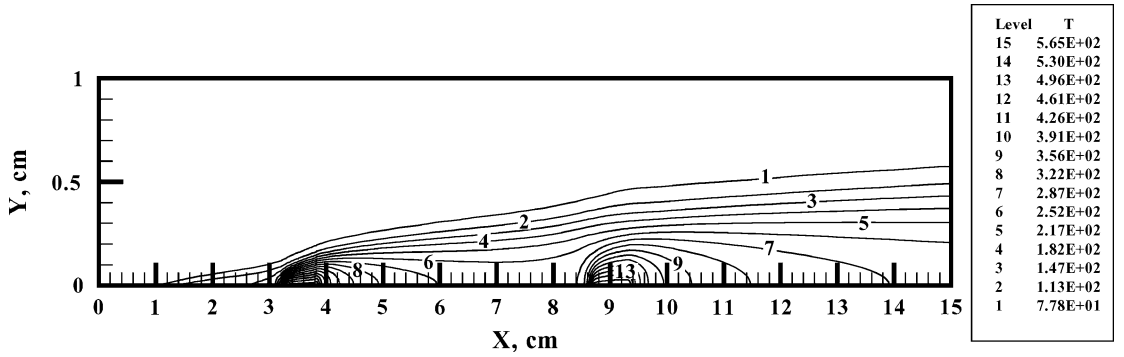

Fig. 7 Temperature contour over glow discharge field, T in K.

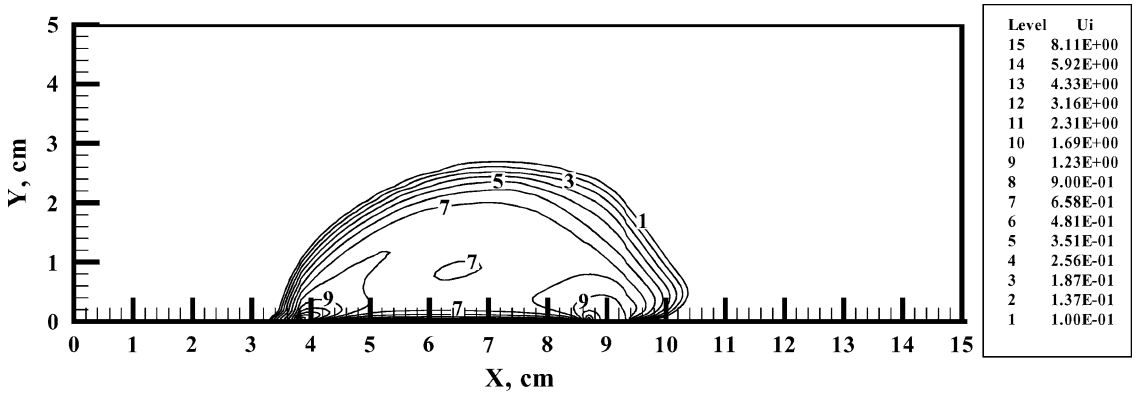

Fig. 8 Charged particle number concentration over the electrodes, 10^{10} cm^{-3}.

surface pressure by the glow discharge is in good agreement with experimental observations.[16]

The corresponding temperature contours over the plate are depicted in Fig. 7. The temperature distributions represent the result of heat transfer by conductive, convective, and Joule heating in the boundary layer. The high-temperature regions downstream of the electrode and within the discharge domain correctly reveal the anticipated physical phenomenon. Preliminary verification by comparing with experimental observation exhibits a general agreement in the overall temperature distributions over the electrodes. Additional and detailed comparison must be wait for further progress in the experimental effort.

Figure 8 gives the ion concentration over the plate in a hypersonic stream. The high-charged particle number density regions are located directly over the electrodes. The local charged particle number density at a distance 0.5 mm above the cathode is 8.11 times greater than the value between electrodes. This behavior is well known both from experiments[15,16] and from the previous numerical simulation based on the drift-diffusion glow discharge model.[18,19] The charge particles are highly constricted in the discharge path between electrodes by the electric field. Most importantly, the charged particle number density is in excellent agreement with the experiment that was conducted at the identical testing condition. The charged particle number density within the glow discharge path has a range from 10^{10} to 8.11×10^{10}/cm^3. In fact, the computed ion number density profiles over electrodes are within the scattering band between Langmuir probe and microwave absorption measurements. The maximum measured ion number density is determined to be in the range of $3.0 \times 10^{11} \sim 1.9 \times 10^{12}$/cm^3 (Refs. 15 and 16).

The numerical simulation has the ability to single out the heat transfer from different mechanisms. The Joule heating is quantified in Fig. 9. The energy conversion process takes place along the discharge path including the plasma sheath, and the most intensive Joule heating is located over electrodes. The relative magnitude of Joule heating and the conductive heat flux over the anode has a ratio of 1.125 (for the model 1). The computed result shows that Joule

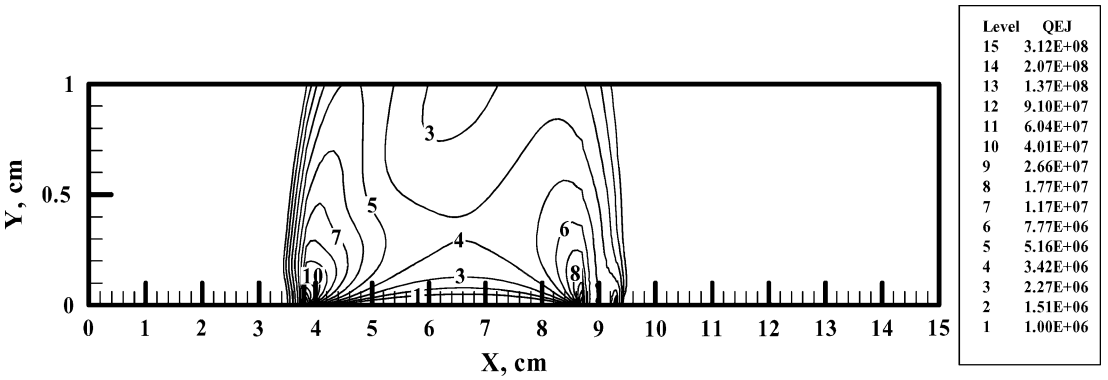

Fig. 9 Joule heating over the electrode embedded plate, erg/cm^3 s.

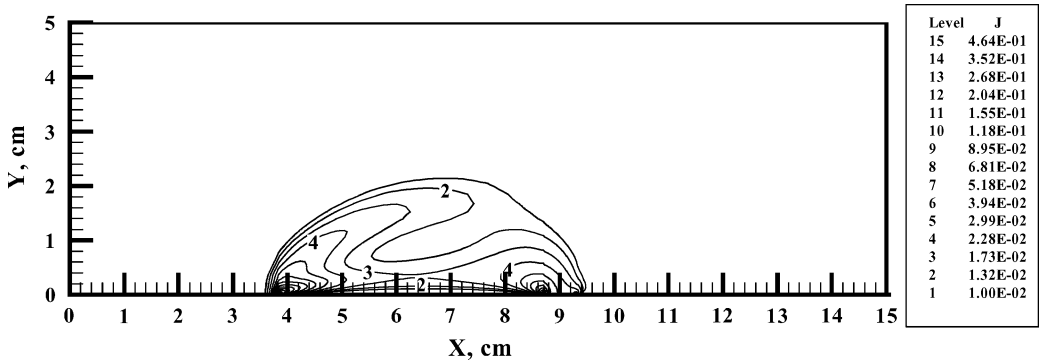

Fig. 10 Electric current density of the glow discharge, mA/cm^2.

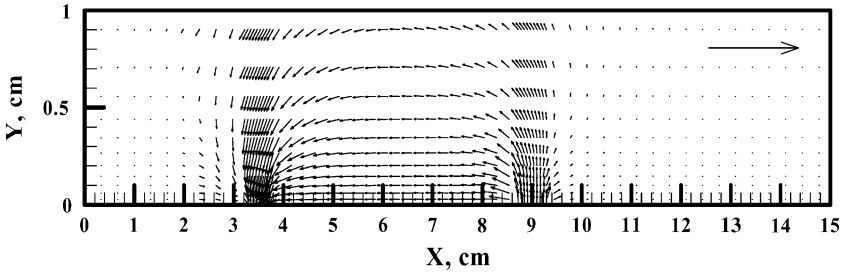

Fig. 11 *E*/emf; reference vector value of emf/R_{dim}; R_{dim} = 5 cm.

heating makes a significant contribution to modifying the boundary-layer structure, especially over the electrodes.

From the calculated electric current density, the behavior of Joule heating in the glow discharge is easily understood. The current density contours of the discharge are presented in Fig. 10. The electrical current density of the glow discharge is presented in the physical dimension of mA per cm^2. The lower current density contours in the discharge region reveal a rather intriguing pattern. But the electric current density is nearly constant away from the electrodes. The high current density region is located immediately adjacent to electrodes. The highly concentrated discharge current path between electrodes is restrained deeply within the plasma sheath over the dielectric model surface.

The electric field intensity is depicted in a vector field format; the reference vector is given in terms of the emf over a reference length of 5 cm. The electric field intensity varies gradually across the electrode, but exhibits rapid change in the cathode fall region, Fig. 11. Over a major portion of the electrodes, the electric field vector is mostly perpendicular to the discharging surfaces. It is understandable that the maximum Joule heating coincides with the highest electric field intensity in the discharge path.

The verification of the present computational results is obtained by comparison with experimental data. For the present purpose, the validation is limited only to the surface-pressure measurements.[15,16] Figure 12 depicts the comparison of surface pressure distributions on the second model with the actuated dc glow discharge. The surface discharge is generated by a constant electrical current of 50 mA at a nominal power supply voltage of 1.2 kV. This simple dc glow discharge modifies the boundary-layer structure and leads to an ensuing viscous-inviscid interaction. As a direct consequence, the surface pressure increases above the value predicted by classic pressure interaction theory.[17] Equally important, very good agreement has been reached between experimental and computational results.

The electromagnetic effect enters into the shock-boundary-layer interaction by modifying the boundary-layer profile. The basic mechanisms are the electrode and Joule heating and the Lorentz force; at very low density, the Hall effect and ion slip can be also added to the list of significant mechanisms.[11,12] Although in principle the electrode heating can also be generated by electric resistance alone, the response time and intensity are substantially slower than the dc discharge. The Joule heating and the Lorentz force exerted on the boundary have strictly electromagnetic origins. The intensity of Joule heating in the present drift-diffusion gas discharge model is regulated by the electric field intensity and the discharge current density via the external circuit equation. To a lesser degree, the energy released into the boundary layer is also proportional to the electrode temperature.

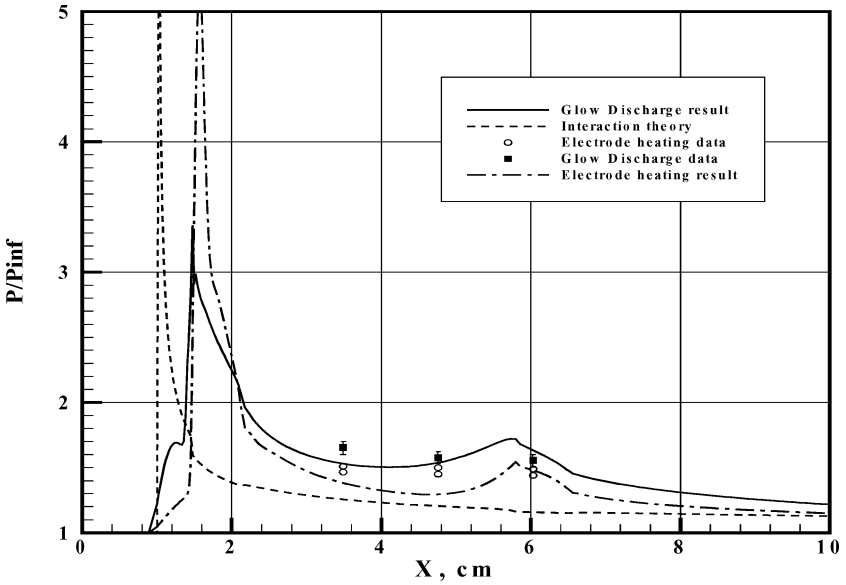

Fig. 12 Induced pressure interaction with and without dc glow discharge.

The contribution from the Joule heating can be separated from electrode heating in the computation. To demonstrate the electromagnetic effect on the induced pressure interaction, the pressure distributions produced both by the glow discharge and electrode heating are depicted in Fig. 12. Both calculations were conducted at the identical electrode surface temperature of 600 K (Refs. 15 and 16). In this comparative study, the glow discharge heating contains the conductive heating from the electrodes, in addition to the Joule heating. From this comparison, it is clearly revealed that the Joule heating, a volumetric heat source, makes further modification to the displacement thickness of the boundary layer beyond the electrode heating. At higher electrode surface temperatures, the electrical current density and the induced pressure are elevated accordingly.

As a direct comparison, the surface-pressure measurements over a plate at the identical flow condition are also included in Fig. 12. In the experiment, the electrodes were heated by an electrical resistor with the total power supply of 50 W matching the power generated by the glow discharge. The open circle symbols designate the surface pressure data by electrode heating alone.[15,16] The surface data collected for the glow discharge are given by the filled square symbols. The computational and experimental results have reached good agreement and show that the glow discharge is much more effective in modifying the boundary-layer structure than the electrode heating. More importantly, the volumetric Joule heating is almost instantaneous in contrast to the slower response of the electrode surface heat transfer. In short, the present result has shown for the first time that the electromagnetic force in the form of a surface plasma can be used as a hypersonic magnetoaerodynamic actuator.

Electromagnetic Interactions

Up to this point, the magnetoaerodynamic actuator exclusively used the embedded electrode and Joule heating to generate the induced pressure interaction. The Lorentz force or the applied magnetic field can further modify the flow near the surface, thus controlling the boundary-layer structure.[7,11] The magnetic field is known to significantly suppress electron mobility and introduces the Hall effect.[11,12] Under the present experimental condition with a transverse magnetic field of $B = 0.2$ T, the electron cyclotron and the electron-neutral collision frequency is estimated to be 3.5×10^{10} rad/s and 6.3×10^{9} s^{-1}, respectively. The Hall parameter is 5.6 rad to indicate a nearly collisionless environment, in which the ion-slip phenomenon can also be dominant. Under this condition, the electric field E is still overwhelmed by the $[\boldsymbol{V} \times \boldsymbol{B}]$ acceleration. In addition, the presence of a magnetic field does not allow steady and uniform plasma.

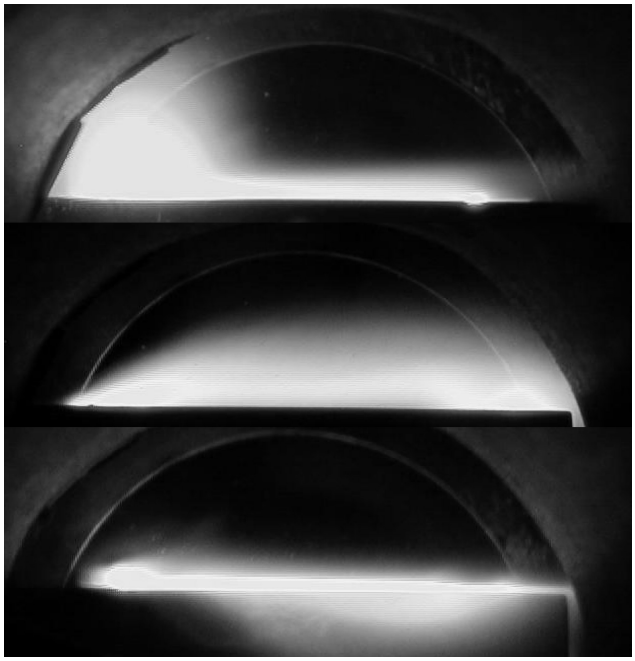

Fig. 13 Glow discharge affected by the applied external magnetic fields ($B = 0$, $B = +0.2$ T $J \times B > 0$, $B = -0.2$ T $J \times B < 0$).

In the present investigation, a constant transverse magnetic field across the surface plasma generates a Lorentz force. The applied external magnetic field is parallel to the embedded electrode surface and perpendicular to the airflow over the model. The positive polarity of the applied magnetic field designates that the field is applied in an orientation from the left to the right side of the flow. The magnetic field of the positive polarity exerts a net uplifting Lorentz force on the electrons. Through collision processes between ions and neutral particles, the Lorentz force thickens the displacement thickness in addition to the electrode and Joule heating. By reversing the polarity of the applied magnetic field, the modification of the boundary layer counteracts the heating effect to thinning the displacement thickness. The induced change in surface-pressure distribution by the electromagnetic field might not be substantial in the electric field dominated glow discharge, but the ensuing inviscid-viscous interaction greatly amplifies the perturbation in a hypersonic stream. In Fig. 13, these phenomena are clearly observable in a composite

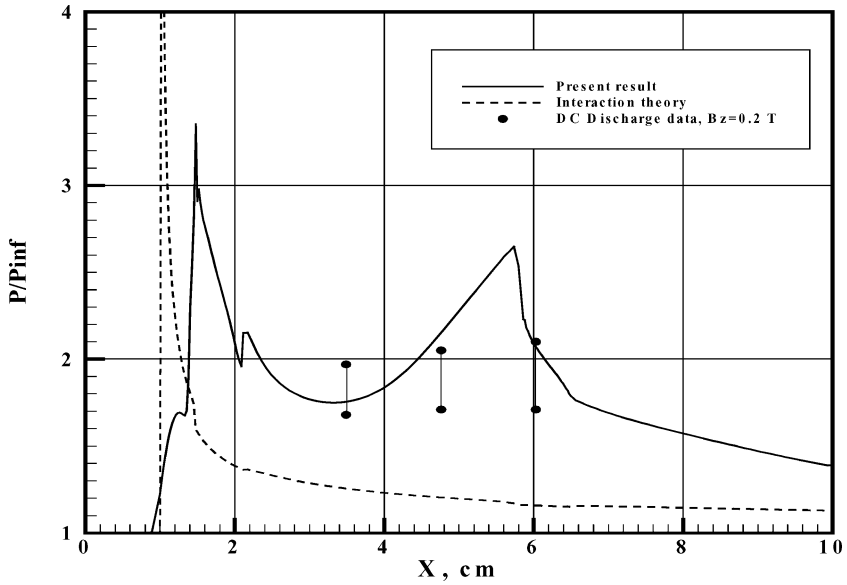

Fig. 14 Induced surface pressure by electromagnetic field, $B = +0.2$ T.

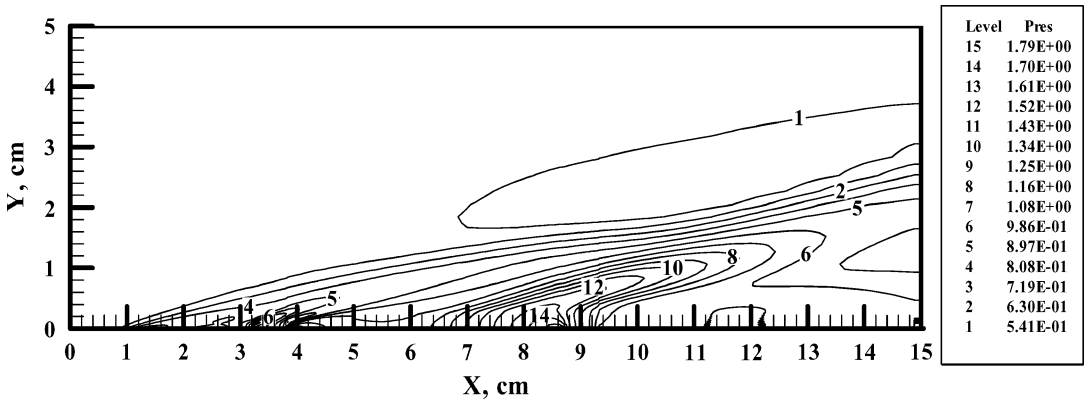

Fig. 15 Pressure contour of magnetoaerodynamic interaction, $B = +0.2$ T.

photograph of glow discharges in the presence of magnetic flux density of $B = 0, +0.2$, and -0.2 T. In the presence of an externally applied magnetic field, the illuminating region over the cathode is substantially suppressed toward the downstream anode.

In the present numerical simulation, the magnetic field strength of $0.1 \sim 0.2$ T is considered. Figure 14 describe the induced pressure by electrode and Joule heating as well as the uplifting Lorentz force by an applied external magnetic field. The external magnetic field with a flux density of 0.2 T was applied with positive polarity to produce the Lorentz force that enhances the inviscid-viscous interaction. The glow discharge was still maintained an electrical potential field of 1.2 kV and with a resistance of 12 kΩ in the discharge circuit. As mentioned earlier, the electrode surface temperatures are assigned a value of 600 K. The agreement between computational and experimental results is reasonable. Under the strong magnetic field strength the surface-pressure data exhibit substantial oscillations reflected by a wide scattering band in the data. From this comparison with measurements, it is observed that an applied magnetic field produces a substantial modification to the structure of the interacting boundary layer. In short, the Lorentz force has enlarged the domain of influence far upstream to the leading edge of the plate. The perturbation of the electromagnetic force further amplifies the viscous-inviscid interaction and significantly increases the induced surface pressure in comparison to the effect of electrode and glow discharge alone.

The pressure contours for the induced viscous-inviscid interaction utilizing the electromagnetic force including the Joule heating and the Lorentz force are depicted in Fig. 15. The complex shock-waves system corresponds perfectly with the surface-pressure distribution. Indeed, the magnetoaerodynamic interaction induced compression waves are merged with the leading edge shock as it is observed in this figure.

Figure 16 depicts the charged particle number density distribution over the plate with a magnetic field intensity of $B = +0.2$ T. The ion number density is lower than the discharge in the absence of an externally applied magnetic field; the maximum computed value is reduced from $8.11 \times 10^{10}/\text{cm}^3$ to $6.16 \times 10^{10}/\text{cm}^3$. The computed results reflect correctly that the applied magnetic field indeed suppresses the mobility of the charged particles. In spite of that, the Lorentz force moves the charged particle path outward from the plasma sheath region; however, the overall dimension of the discharge region remains nearly unaltered. The charged particles are now concentrated near the electrodes, where they are constricted by the strong magnetic forces.

By reversing the polarity of the applied magnetic field, a counteractive effect is observed by Joule heating and the compressing Lorentz force. For this computation, the applied external field is limited to a magnetic field flux density of 0.2 T to maintain the computational stability. In Fig. 17, the comparison with surface-pressure measurements only indicates a general agreement. The computational result shows a more pronounced influence by the applied magnetic field than that of experimental data. Both the numerical results and experimental measurements revealed different degrees of unsteadiness. In addition, the assumption of a two-dimensional interacting flow is seriously challenged. The calculated and measured

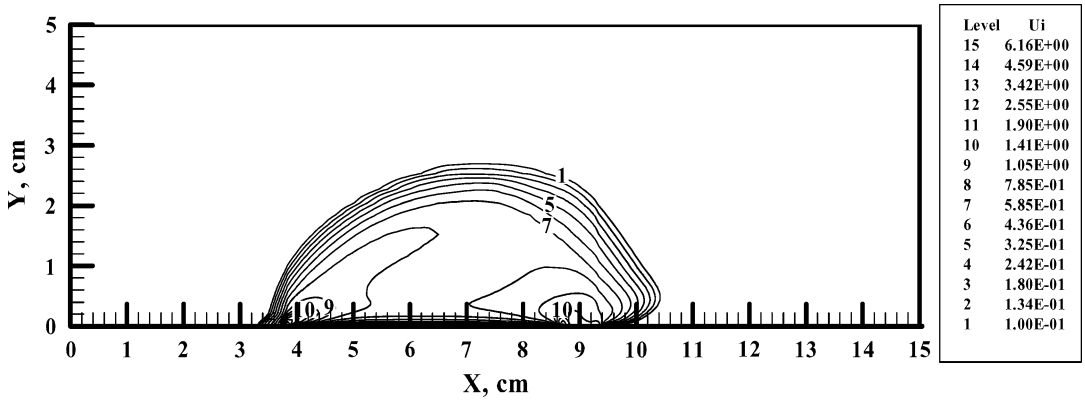

Fig. 16 Charge particles distribution, 10^{10} cm^{-3}, with $B = +0.2$ T.

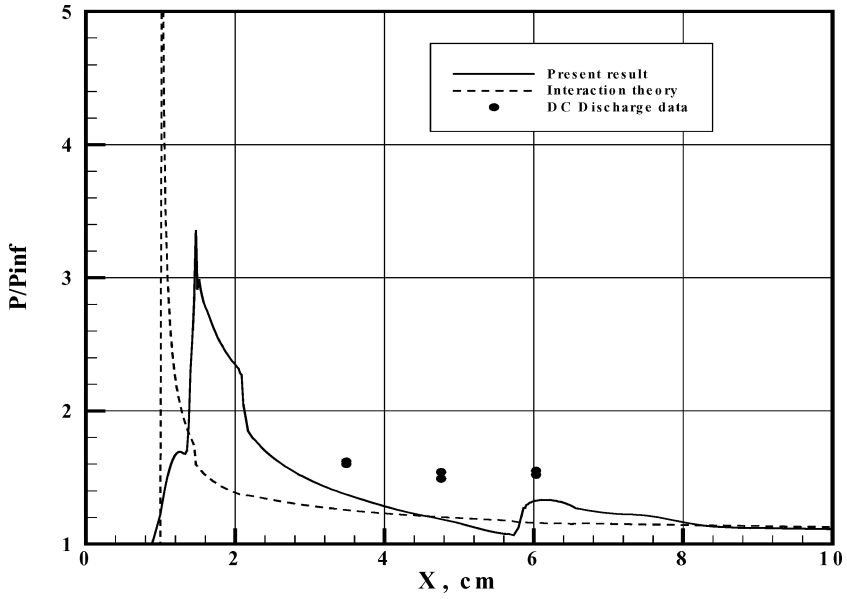

Fig. 17 Surface-pressure distribution over plate, $B = -0.2$ T.

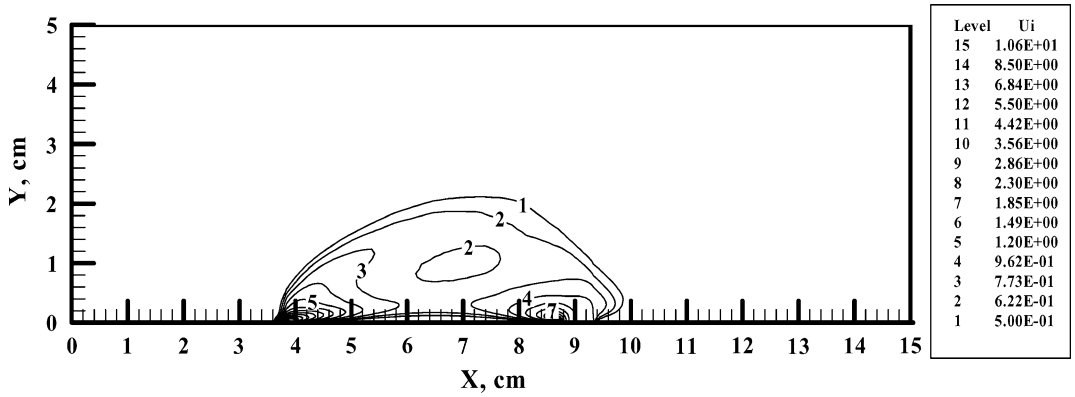

Fig. 18 Charged particle distribution, 10^{10} cm^{-3}, with $B = -0.2$ T.

induced surface pressure with magnetoaerodynamic interaction is noticeably subdued, and the applied magnetic field has fundamentally altered the flowfield structure in that the interacting flow in the magnetic field has an expanded domain of influence and reaches forward to the leading edge of the plate.

The general features of the pressure contours and the thermal field for the reversed magnetic polarity ($J \times B < 0.0$) are similar to that of the positive polarity ($J \times B > 0.0$) and therefore are not presented here. Again, the applied external magnetic field has shown a profound effect on the electrodynamic structure of the glow discharge. This observation, reinforced by calculations, includes both polarities of the magnetic field. A systematic experimental effort, although extremely demanding, is in process. Figure 18 depicts the reduced charged particle distribution around the electrodes by the suppressing Lorentz force, $B = -0.2$ T. The diminishing effect on the diffusion and the drift motion of the charged

particles are clearly demonstrated. This profound change of the discharge pattern seems to be independent of the polarity of the applied field. Furthermore, the glow discharge under the influence of an externally applied magnetic field exhibits highly unstable behavior both from the experimental and computational observation. The basic characteristics of the magnetoaerodynamic interaction are time dependent and three dimensional, thus beyond the scope of the present analysis. The verification of the concept for the magnetoaerodynamic actuator involves a huge parametric space for engineering applications. Therefore, the present comparative study between experiments and computations must be limited to global behavior of aerodynamic performance parameters such as C_p and C_f.

Nevertheless, all numerical simulations reveal that the basic concept for flow control using surface plasma as the trigger mechanism and amplifying by an ensuing viscous-inviscid interaction is a viable technical innovation. Additional verification of the drift-diffusion glow discharge model together with computational accuracy is still required. The progression toward the three-dimensional computational simulation is the next most critical requirement for validating the physical fidelity.

Conclusions

Numerical simulations have been successfully demonstrated a surface plasma to be an innovative hypersonic flow control actuating surface as a perturbation to the flowfield and subsequent amplifying by a viscous-inviscid interaction. The basic premise of the magnetoaerodynamics actuator has also been substantiated by preliminary experimental measurements. The present approach has the potential to replace a traditional hypersonic flight control system using an actuator, servomechanism, and moving control surfaces by a simple segmented electrode embedded in the fixed control surface.

The drift-diffusion model for the glow discharge has been applied successfully to describing the surface discharge phenomena. Numerical results have also shown that Joule heating in the glow discharge is not necessarily always producing the detrimental effect as it does in many applications. The applied external magnetic field reveals profound impact to the electrodynamic structure and therefore enhances the ensuing viscous-inviscid interaction.

The present numerical results are only partially verified by the preliminary side-by-side experimental observations. The detailed quantification of the effectiveness of the control mechanism must be sustained to reach fruition.

Acknowledgments

The sponsorship of D. Paul and R. Melville of the Air Force Research Laboratory is sincerely acknowledged. The invaluable contributions in experimental efforts by R. Kimmel and J. Hayes of the Air Force Research Laboratory and J. Menart of Wright State University are sincerely appreciated.

References

[1]Ganiev, Y., Gordeev, V., Krasilnikov, A., Lagutin, V., Otmennikov, V., and Panasenko, A., "Aerodynamic Drag Reduction by Plasma and Hot-Gas Injection," *Journal of Thermophysics and Heat Transfer*, Vol. 14, No. 1, 2000, pp. 10–17.

[2]Fomin, V., Maslov, A., Malmuth, N., Formichev, V., Shashkin, A., Korotaeva, T., Shipyuk, A., and Pozdnyakov, G., "Influence of a Counterflow Plasma Jet on Supersonic Blunt-Body Pressure," *AIAA Journal*, Vol. 40, No. 6, 2002, pp. 1170–1177.

[3]Kuranov, A., and Sheikin, E., "The Potential of MHD Control for Improving Scramjet Performance," AIAA Paper 99-3535, June 1999.

[4]Jacobsen, L. S., Carter, C. D., and Jackson, T. A., "Toward Plasma-Assisted Ignition in Scramjets," AIAA Paper 2003-0871, Jan. 2003.

[5]Knight, D., "Survey of Aerodynamic Flow Control at High Speed by Energy Deposition," AIAA Paper 2003-0525, Jan. 2003.

[6]Shang, J. S., "Plasma Injection for Hypersonic Blunt Body Drag Reduction," *AIAA Journal*, Vol. 40, No. 6, 2002, pp. 1178–1186.

[7]Shang, J. S., "Recent Research in Magneto-Aerodynamics," *Progress in Aerospace Sciences*, Vol. 37, No. 1, 2002, pp. 1–20.

[8]Leonnov, S., Bityurin, V., Savelkin, K., and Yarantsev, D., "Effect of Electrical Discharge on Separation Processes and Shocks Position in Supersonic Airflow," AIAA Paper 2002-0355, Jan. 2002.

[9]Gaitonde, D. V., "Three-Dimensional Flow-Through Scramjet Simulation with MGD Energy-Bypass," AIAA Paper 2003-0172, Jan. 2003.

[10]Post, M. L., and Corke, T. C., "Separation Control Using Plasma Actuators—Stationary & Oscillating Airfoils," AIAA Paper 2004-0841, Jan. 2004.

[11]Mitchner, M., and Kruger, C., *Partial Ionized Gases*, Wiley, New York, 1973, p. 171.

[12]Raizer, Yu. P., *Gas Discharge Physics*, Springer-Verlag, Berlin, 1991, p. 20.

[13]Raizer, Yu. P., and Surzhikov, S. T., "Two-Dimensional Structure of the Normal Glow Discharge and the Role of Diffusion in Forming of Cathode and Anode Current Spots," *High Temperatures*, Vol. 26, No. 3, 1988, pp. 304–311.

[14]Surzhikov, S. T., and Shang, J. S., "Glow Discharge in Magnetic Field with Heating of Neutral Gas," AIAA Paper 2003-3654, June 2003.

[15]Kimmel, R., Hayes, J., Menart, J., Shang, S., Henderson, S., and Kurpik, A., "Measurements of a Transverse DC Discharge in a Mach 5 Flow," AIAA Paper 2003-3855, June 2003.

[16]Menart, J., Shang, J. S., Kimmel, R., and Hayes, J., "Effect of Magnetic Fields on Plasma Generated in a Mach 5 Wind Tunnel," AIAA Paper 2003-4165, June 2003.

[17]Hayes, W., and Probstein, R., *Hypersonic Flow Theory*, Academic Press, New York, 1959, pp. 333–374.

[18]Surzhikov, S. T., and Shang, J. S., "Supersonic Internal Flows with Gas Discharge and External Magnetic Field," AIAA Paper 2003-3625, June 2003.

[19]Surzhikov, S. T., and Shang, J. S., "Numerical Simulation of Subsonic Gas Flows with Gas Discharge and Magnetic Field," AIAA Paper 2003-3759, June 2003.

[20]Chen, F. F., *Introduction to Plasma Physics*, Plenum, New York, 1974, Chap. 2.

[21]van Leer, B., "Towards the Ultimate Consideration Difference Scheme. V, A Second-Order Sequel to Godunov's Method," *Journal of Computational Physics*, Vol. 135, Aug. 1997, pp. 229–249.

G. Candler
Associate Editor